JOURNAL OF MATERIALS SCIENCE **39** (2004) 6791 – 6805

Scanning electron acoustic microscopy (SEAM): A technique for the detection of contact-induced surface & sub-surface cracks

T. F. PAGE, B. A. SHAW*
*School of Chemical Engineering and Advanced Materials and *Design Unit, School of Mechanical and Systems Engineering, University of Newcastle upon Tyne, Newcastle upon Tyne, NE1 7RU, UK*
E-mail: t.f.page@newcastle.ac.uk

A variant of the scanning acoustic microscopy technique, scanning electron acoustic microscopy (SEAM), uses a pulsed electron beam in a conventional scanning electron microscope (SEM) to generate elastic waves near the surface of the sample. Conveniently for studies of surface damage, the contrast-generating processes are at a depth commensurate with the thickness of many thin hard ceramic coatings and the typical depths of fatigue-induced cracks in both gears and rolling element bearing systems.

Using examples from our studies of contact damage induced in thin hard coated systems and gears, this paper will demonstrate the applicability of SEAM techniques to the study of near-surface damage in coated systems (coating fracture and debonding) and gears (fatigue damage). We show that clear contrast can arise from cracks oriented both parallel to and, sometimes, perpendicular to the surfaces of many samples, and show that useful information can be provided regarding the debonding of coatings. It has also been found possible to delineate sub-surface contact and contact fatigue cracks allowing some information regarding crack orientation and extent to be deduced without the need for either serial or vertical sectioning of the sample.

1. Introduction

In non-transparent solids, it can be difficult to detect either the presence of internal cracks or the sub-surface extent of surface-breaking cracks by conventional techniques, but sometimes these critical defects can be successfully imaged using acoustic techniques of varying resolutions (e.g., standard, bulk, ultrasonic, crack detection methods (non-destructive evaluation (NDE) techniques), scanning acoustic microscopy (SAM) [e.g., 1–3]). A less common variant of the acoustic technique, scanning electron acoustic microscopy (SEAM), uses a pulsed electron beam in a conventional scanning electron microscope (SEM) to generate elastic waves near the surface of the sample. The depth below the surface at which acoustic waves are generated, and from which the majority of image contrast arises, depends on both the electron beam energy and the properties of the sample, but is typically in the range $0 \rightarrow 5$ μm for beam energies of $0 \rightarrow 30$ kV–a figure attractively commensurate with the thickness of many thin hard coatings and the typical depths of fatigue-induced cracks in both gears and rolling element bearing systems.

While SEAM has been available for nearly two decades, and a number of useful applications demonstrated, it appears that the technique has found little applicability in one of the branches of the research community to whom it may be most useful. The purpose of this paper is therefore to demonstrate the potential applicability of the SEAM technique in the areas of contact damage and surface engineering and to encourage others to explore this powerful and promising technique.

As a host for this technique, scanning electron microscopy (SEM) offers a powerful means of characterising materials by utilising the wide range of signals resulting from the interaction of solid samples with a scanning beam of energetic electrons. In this way, a wide range of topographic (e.g., detailed fracture surface shapes), functional (e.g., the dimensions of magnetic domains), microstructural (e.g., the size and shape distributions of phases) and microchemical (e.g., segregation profiles) information can be retrieved, often with sub-micron spatial resolutions [e.g., 4]. An obvious attraction of SEM techniques is the ability to form readily-accessible visual images from the various signals emanating from the sample—for example, surface topography and shape (secondary electron imaging), the mapping of atomic number (z) (backscattered electron imaging), the determination of local crystallographic orientation using either selected area channelling patterns or backscattered electron patterns (backscattered electron imaging), and the determination of local chemical composition (including the detection of light elements down to carbon) using

energy dispersive X-ray analysis (EDX) techniques [e.g., 4–6]. Thus, a further attraction of SEAM is that acoustic imaging can be performed in parallel with other SEM imaging and microanalysis modes, thus enabling the origins of contrast in the acoustic signal to be further identified and characterised [e.g., 5, 7, 8].

However, while any residual electronic charge on the sample (resulting from the scanning electron beam-sample-signal interactions during imaging) is usually conducted away to earth, less readily obvious is the fate of the considerable energy densities being continuously deposited by the beam. Thus, perhaps the least widely known signal is that arising from the elastic ('acoustic') waves which propagate through the sample having originated from the local thermal expansions and contractions necessarily accompanying the deposition and dissipation by 'thermo-elastic conversion' of much of the electron beam energy in the near surface regions of the sample [e.g., 9, 10]. This acoustic signal can also be used to form images and offers a scanning electron acoustic microscopy (SEAM) addition to the usual array of SEM signals. In this way, the microscope can be used in an analogous manner to a scanning acoustic microscope (SAM) to map defects, albeit in a different frequency range (and therefore with some notable differences (see [9, 10] and later)), but with a spatial resolution of a few micrometers. While early SEAM studies focussed on accessing thermal and elastic information in a variety of materials [e.g., 9–12], SAM had some early success in delineating the sub-surface cracks controlling the debonding of metallisation in VLSI systems [e.g., 3, 13] and thus there appeared to be a clear potential for SEAM to reveal similar features, e.g., sub-surface contact-induced defects in coated systems and components damaged by contact fatigue (e.g., bearings and gears). While a few reports of observations of near-surface cracks in a variety of materials have appeared from various authors [e.g., 9, 10, 14, 15], we can now confirm that SEAM has significant applicability in studies of near-surface damage and surface-engineered systems, and is especially apposite since the depth-sensitivity of the technique is of a spatial scale commensurate with that necessary for such studies (see later).

The essential layout of a SEAM-SEM is shown in Fig. 1. The SEM sample is mounted in intimate contact with an acoustic transducer (usually a thin slice of lead zirconium titanate (PZT)) which is used to generate an oscillating electrical signal from the vibrations of the sample itself. The beam is then not only scanned across the sample in the usual way but also modulated by a beam-blanking system in the electron column (often immediately below the electron gun). This system needs to possess a fast rise-time (∼1–2 ns) so that it can modulate or 'chop' the beam at frequencies corresponding to the resonant frequencies of the sample/holder system for elastic waves travelling through the sample and across the sample surface (Love and Rayleigh waves). These frequencies depend on the sample/holder size etc. but are typically of the order of 100 MHz−2 GHz [e.g., 9, 10]. The resulting acoustic signals are isolated by a phase-locked amplifier (running synchronously with the beam modulation) which is necessary to enhance the sensitivity of the detection system for the low signal strengths involved. The output of the phase-lock amplifier is then fed into the video chain in the normal way for the purpose of creating images.

Some of the earliest images to demonstrate the possibilities of SEAM imaging for materials characterisation were those by Cargill [16] and Rosencwaig [17] who, for example, were able to reveal the immediate sub-surface grain structure in an abraded stainless steel

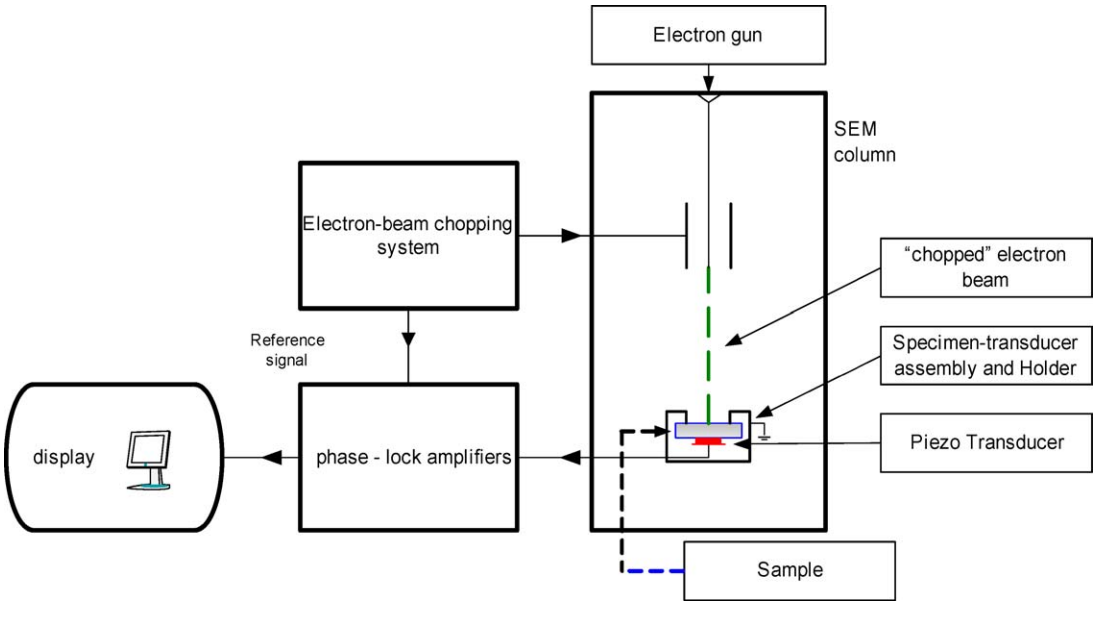

Figure 1 A schematic representation of the elements of the Scanning Electron Acoustic Microscopy (SEAM) adaptation of a SEM (after [9]). The SEM column is modified to accommodate an electron beam modulation system (usually mounted just below the gun and consisting of a compact parallel-plate condenser assembly through which the beam passes and can be deflected with a rise time of ∼a few ns) and a special sample holder in which the sample is in intimate contact with a piezzo-electric detector (usually a PZT crystal). The output from the transducer is fed through a local pre-amplifier to a phase-lock amplifier (referenced to the beam modulation system) and then to the main video display system where it can be recorded in parallel with conventional secondary and back-scattered images, X-ray maps etc.

sample whose surface microstructure was totally obscured by scratches, while Rosencwaig and White [18] and Thomas, Farrow and Joy [19] were able to demonstrate that the SEAM signal could be used to detect changes in the thermal conductivity of thin ($\sim$1 μm) ion-implanted near-surface layers in silicon as a function of radiation damage. Subsequently, both Davies [9] and Balk and co-workers [e.g., 10] have established the technique further and showed how signals can best be detected and processed under a wide variety of conditions to extract a wide range of materials information from the sample [e.g., 9, 10, 15]. Thus it has been clearly established that SEAM contrast can arise from differences in density and elastic moduli, differences in thermal expansion coefficient, differences in thermal conductivity, stress concentrations (including the localised stresses associated both with dislocation arrays and with magnetic domains though magnetostriction) [e.g., 9–15].

While the detailed principles of SEAM have been well-described previously in the literature [e.g., 9, 10], widespread application of the technique has probably been hindered both by the need to add further hardware to the SEM system (including a potentially expensive beam blanking insert in the column) and the complexity of quantitatively modelling the thermoelastic conversion process in order to fully establish a working contrast theory to fully explain the various types of sample information revealed by this imaging method. Thus contrast theories remain largely qualitative and empirical. Despite these problems, it is surprising that the technique has not found more widespread use in studies of surface damage and surface engineering.

2. Depth-sensitivity of SEAM: The scale of information retrieval

Two effects are critical in determining contrast in the SEAM imaging mode—the first is the generation of acoustic waves by the energy deposited by the electron beam in the sample (the thermoelastic conversion), while the other is the propagation of these elastic waves through the remainder of the sample to the detector (which is usually mounted on the lower surface of the specimen as shown in Fig. 1). Fig. 2 demonstrates schematically that when the acoustic wavelength is large (e.g., a few mm) compared to the sample thickness, contrast is dominated by the generation of the acoustic wave (as in SEAM); under these conditions the majority of the sample depth beyond the generation depth, t_c, adds little else to the contrast, and the acoustic waves simply act to carry information from the generation volume to the detector. However, as the wavelength becomes shorter, it is the propagation of the acoustic signal which is critical (as in SAM) and under these conditions further contrast can arise from features throughout the sample thickness. The beam chopping frequencies typically used in SEAM (100 s kHz) create wavelengths between these extremes, that is closer to the long wavelength condition. Thus SEAM has an intrinsic sensitivity to near-surface features, which is crucial to our surface contact damage and thin film coating studies.

The value of t_c (the 'thermo-elastic conversion depth') is determined by the sample properties, the beam energy (both of which jointly control the electron range (β) in the sample) and the beam chopping frequency [9, 10]. Thus, t_c acts as the near-surface cut-off distance for the efficient detection of any sub-surface

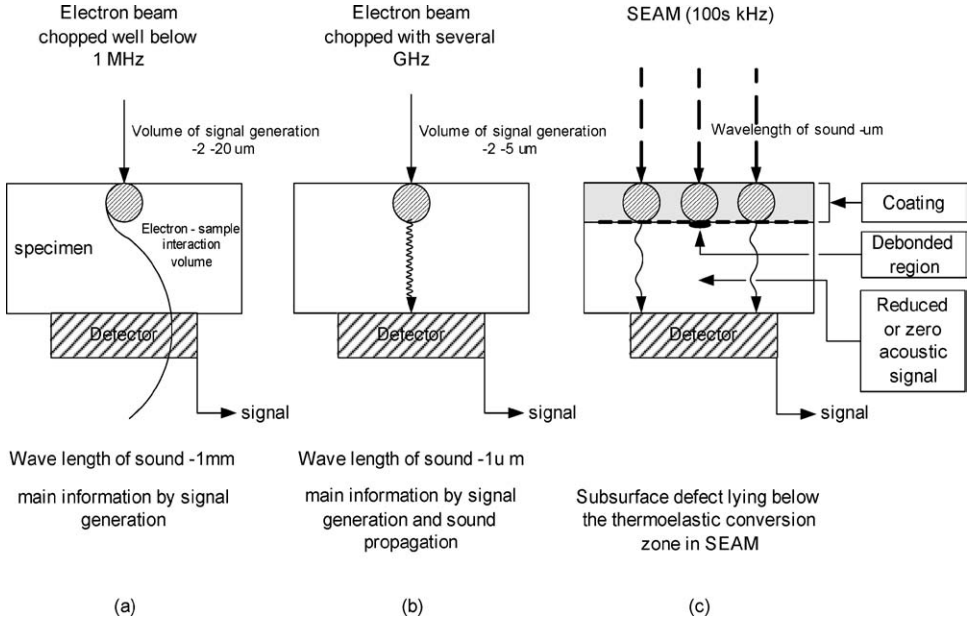

Figure 2 A schematic representation of the generation of contrast in SEAM (after [10]). (a) At low modulation frequencies, and hence wave-lengths which are long compared to the sample thickness (as in SEAM), contrast is dominated by sample features occurring in the thermo-elastic conversion volume. (b) As the modulation frequency is raised towards that conventionally used for SAM ($\sim$few GHz), the resultant acoustic wavelength becomes small compared to the sample thickness and further contrast can arise from specimen features interfering with the wave propagation through the entire sample volume after the thermoelastic conversion. SEAM is closer to (a) than (b) and thus has an intrinsic enhanced sensitivity to defects located at, or about, the electron beam range in the solid (typically 1–5 μm and varying with E_o and ρ etc.). This is demonstrated in (c) where little signal is transmitted beyond the region of coating debond.

defects and is usually slightly less than the electron range (i.e., $t_c \leq \beta$). In principle, all defects lying between t_c and the detector can produce contrast but, as shown in Fig. 2, in SEAM this effect is small compared to the dominant contrast produced by features in the signal generation region. Thus defects lying at $\sim t_c$ below the surface are expected to produce most contrast, with defects lying closer to the surface than t_c only producing weak contrast depending on the efficacy of the thermo-elastic conversion near the surface while those further into the sample cause little perturbation to the long-wavelength elastic waves travelling to the detector. Since β decreases with incident beam energy, a low accelerating voltage is beneficial in resolving defects very close to the scanned surface, but in practice a large accelerating voltage is usually required to give sufficient gun brightness to generate the $\sim 0.4 \times 10^{-6}$ A probe current necessary to generate sufficient signal levels to be detected above the noise in the system thus allowing imaging in reasonable acquisition times (i.e., <several minutes).

Practically, the magnitude of t_c can be approximated to the electron range (β) [9] which itself can be estimated simply by the formula due to Bethe [e.g., 4, 20] i.e.,

$$\beta \approx \frac{33 \times 10^{-2} (E_o)^2}{\rho} \mu\text{m} \quad (1)$$

where E_o is in kV and ρ is the sample density in Mgm^{-3}. Thus $\beta \sim 1$ μm for Fe at $E_o = 30$ kV or SiC at 10 kV, but ~ 9 μm for SiC at 30 kV (see Table I).

Alternatively, PC-based Monte Carlo calculations can be used to estimate β as a function of the beam accelerating voltage (E_o) [20] and these yield similar values of β of 0–10 μm for many solids for electrons in the 0–40 kV beam energy range. Since, in most cases, β varies approximately with E_o^2, atomic number (z) and density, an additional attraction of the PC method is that it is simple to calculate β as a function of E_o, z and ρ and thus select an appropriate value of E_o for the depths and materials involved. Alternatively a value of E_o can be determined experimentally at which maximum contrast occurs from, say, coating debonding.

Experimental observations support the view that the maximum sensitivity to many microstructural defects–including cracks–occurs near t_c and the elastic waves begin their passage through the solid. Thus for

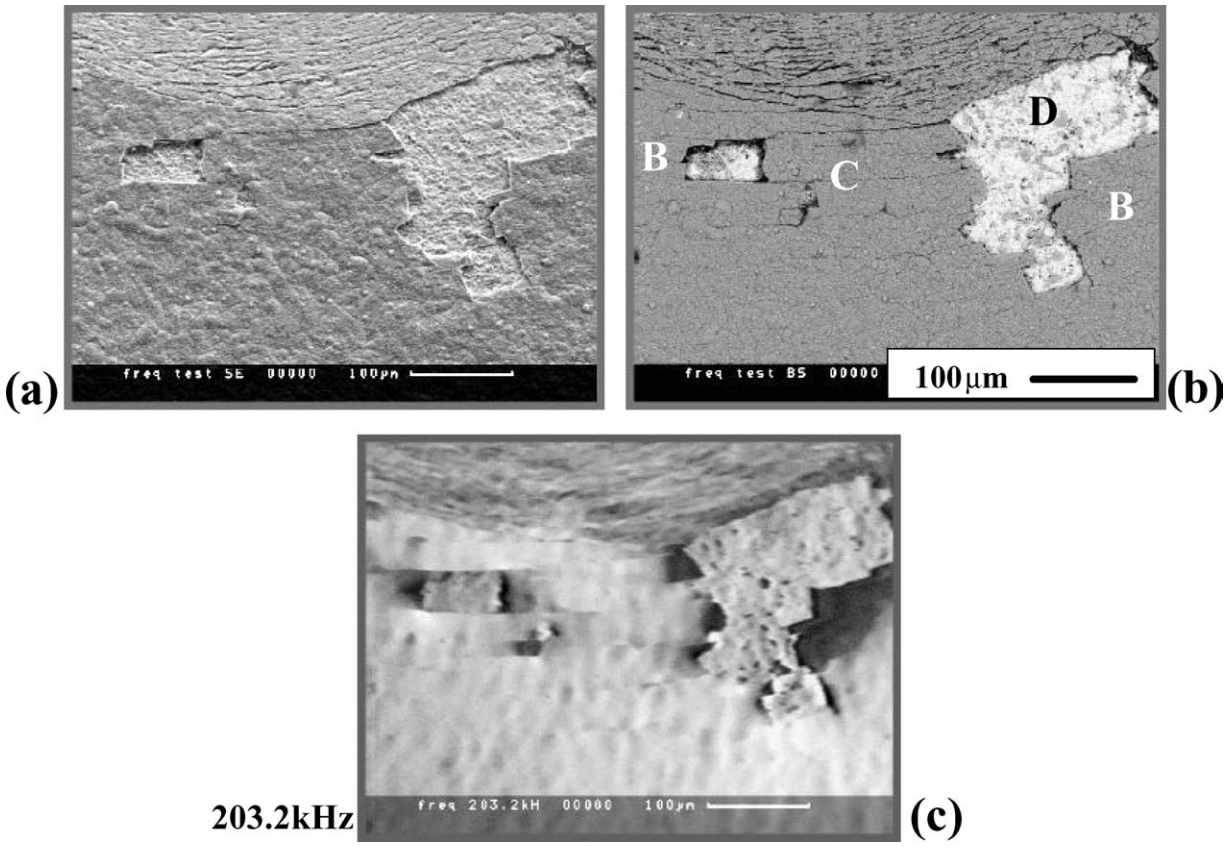

Figure 3 A sample of a thin (~ 5 μm) TiN coating on tool steel examined after a contact damage experiment with a loaded WC ball indenter. The circular indentation site is above the upper edge of each figure with the circumferential array of cracks within the contact site being clearly visible in the upper portion of each figure. Some circumferential (through-thickness) cracking, together with debonding of the coating, is visible in the area shown which has been selected from around the periphery of each indentation. The three micrographs are taken using different signals from the same area [5, 8]. (a) a secondary electron (SE) topographic image showing the surface topography and coating spallation around the damage site; (b) a back-scattered electron (BSE) image in which atomic number contrast reveals the TiN as grey with the steel substrate (revealed by coating spallation) imaging lighter; (c) a SEAM image (203.2 MHz, 25 kV, $\beta \sim 3$ μm) now revealing the full extent of interfacial debonding (dark contrast at areas corresponding to B in Fig. b) and loose (dark) TiN particles on the exposed steel surface. TiN fragments either well-bonded to the steel surface or too thin to create significant thermoelastic conversion contrast (i.e., thickness $\ll \beta$) exhibit no contrast—compare the number of particles visible on the exposed steel surface at D in Fig. b and c, where many do not show contrast. Some through-thickness cracking (e.g., C in Fig. b) (circumferential to the contact site) is also apparent in both the BSE SEAM images.

TABLE I Typical output of PC-based Monte Carlo programs for modelling the spatial distribution of electron-solid interactions in samples being examined by SEM [20, 23]. In this case, the electron range is shown as a function of accelerating voltage, E_o, for two materials of different atomic number and density—one a typical substrate, one a thin hard coating

Material	Atomic no Z	Density (Mgm^{-3})	Range (μm) for a given operating voltage ($E_o = 1, 5 \ldots 40$ kV)							
			1	5	10	15	20	25	30	40
Steel (Fe)	26	7.8	0.02	0.18	0.6	1.1	1.8	2.7	3.7	6.2
SiC	10	3.2	0.02	0.3	1.0	2.1	3.5	5.2	7.2	12.0

coatings in the thickness range 1–5 μm, this distance is easily estimated from simple Monte Carlo calculations and a suitable beam voltage can be chosen.

Readers requiring a more detailed account of the physics of the thermoelastic conversion process, together with contrast models which indicate the sensitivity of the process to a number of contrast-producing parameters, are guided to the excellent summaries by Davies [9] and Balk [10]. However the following additional comments may be useful for intending users of the technique.

As predicted by theory and confirmed experimentally [e.g., 9, 10, 21], there is considerable enhancement in resolution by increasing the chopping frequency into the megahertz range, at least for medium or good thermal conductors. Generally, the resolution varies as $(\text{frequency})^{-1/2}$. Thus in order to improve the resolution to 1 μm or less, either the frequency must be raised (though this is largely dictated by the sample geometry) or β decreased by lowering the accelerating voltage, though (as noted earlier) limits on gun brightness usually impose an experimental lower limit on this of 15–20 kV.

Contrast from one point on the specimen to another is generally due to both amplitude and phase differences (differential signal delays) which can result in phase shifts of any value in the range $0 \rightarrow 2\pi$ [9, 10]. These are observable with the phase-sensitive amplifier

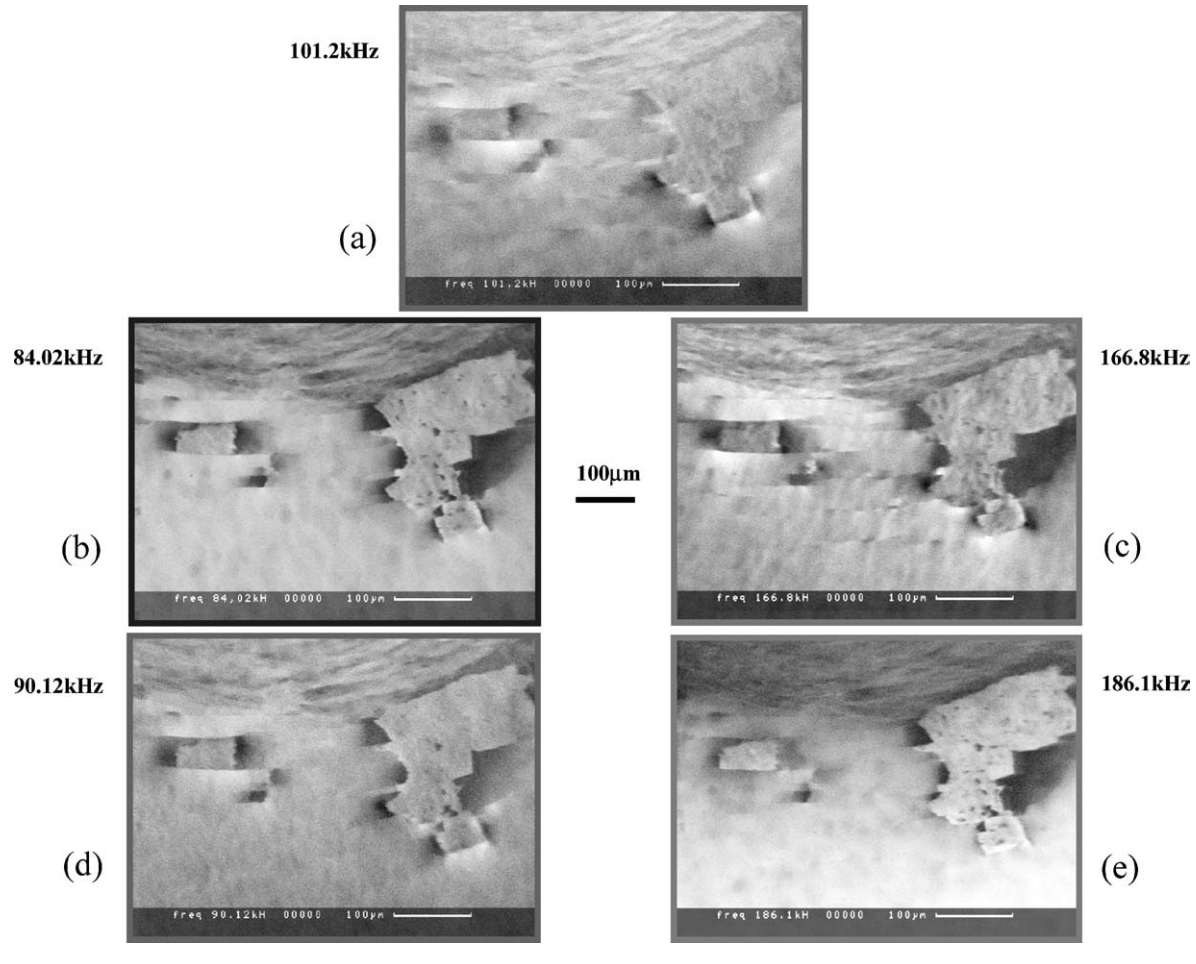

Figure 4 Further SEAM images of the damage area are shown in Fig. 3c but using SEAM signals at different beam-modulation frequencies. Five images have been chosen at which strong SEAM signals occurred, these being (a) 101.2 kHz (∼half the modulation frequency of Fig. 3c); (b) ∼84 kHz and (d) ∼90 kHz and their first multiples; (c) ∼166 kHz and (e) 186 kHz [24]. It is interesting to note that the image contrast varies considerably between these five images, not only in the extent of the debonded area revealed beneath the coating (almost invisible in (a)) but also in the way in which the amount of loose debris is revealed (or not) and also with the delineation of surface-breaking through-thickness cracks—both these latter effects involving contrast being generated very close to the surface (i.e., at depths $\ll t_c$). In all cases, the higher frequency image of each pair tends to reveal the clearer contrast from features nearer the surface (see text). Of the six SEAM images shown of this area in Figs. 3 and 4, Fig. 3c was chosen as having the highest information content regarding coating debonding, through-thickness cracking and the delineation of loose debris.

used, and thus absolute phase measurements are not practicable as such unpredictable phase variations can be induced over a lateral scale of a few millimetres. However, images having phase contrast can show surprising changes in appearance with frequency variations of less than 1%. As Davies has commented [9], what is important is that contrast occurs, not its absolute sign.

Both Davies and Balk [9, 10] have shown how further useful contrast effects can be generated by setting the detection phase-lock frequency to both multiples and odd harmonics of the modulation frequency. However, in this paper we will be only concerned with observations made at given drive frequencies and simple multiples (harmonics) thereof.

3. Experimental

3.1. The instrument

The SEM used in this study has been described in detail elsewhere [5, 7] and was set up for the specific study of ceramic (and other low atomic number (z)) materials. The instrument comprises a Camscan S4-80DV pumped to $\sim 1.10^{-6}$ torr at the specimen and equipped with a specimen airlock (to minimise contamination during the introduction of carefully prepared and cleaned samples). LaB_6 or CeB_6 high brightness sources were used in a gun ion-pumped to $\sim 2 \times 10^{-7}$ torr to produce images in the range of accelerating voltages 500 V–40 kV. An integrating framestore was employed to capture images via a number of detection systems (high sensitivity, silicon back-scattered electron detectors (KE Developments), an Oxford CL system with monochromator, a LINK LZ4/eXL EDX (and image analysis) system and a Cambridge Technology scanning electron acoustic microscopy (SEAM) system). Image storage from the framestore was onto a PC. With this instrument, we have previously demonstrated the satisfactory acquisition of high resolution secondary electron and back-scattered electron images (including electron channelling patterns) at voltages as low as 500 V when image integration is performed through a framestore [5]. Thus, such LaB_6-sourced instruments go some way to decoupling the issues of obtaining good lateral resolution without excessive beam penetration and thus offer the microscopist some of the attractions of field emission sourced systems (FEGSEMs) [22]. In this case, the LaB_6 source is critical in allowing the high probe current necessary for SEAM (~ 1 μA) to be delivered into a ~ 1 μm spot size (approximately by a factor of 10 better than with a conventional W-source and with a total current probably unattainable on most FEGSEMs). Even so, values of $E_o \geq 20$ kV are usually required to generate sufficient gun brightness.

3.2. SEAM adaptation & operation

The essential additional components required for SEAM experimentation are a rapid-response beam

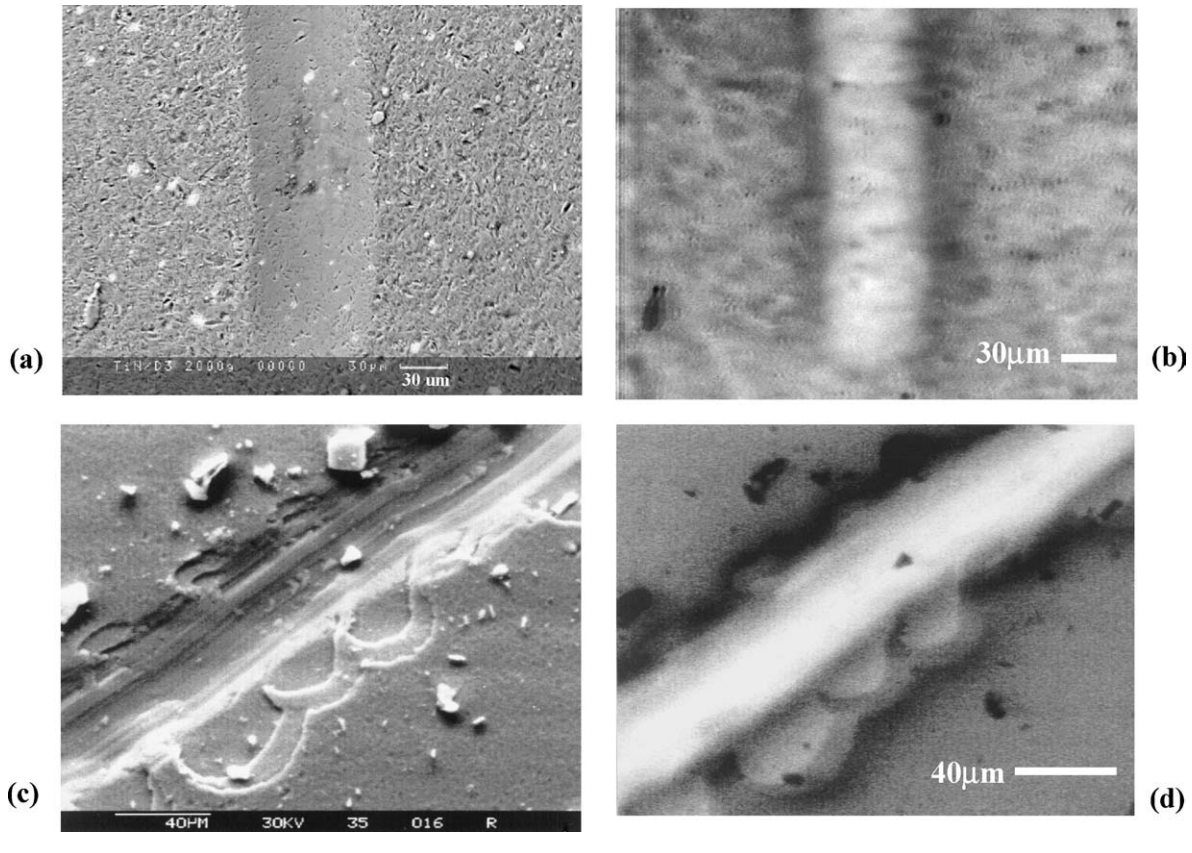

Figure 5 SEAM images of debonding phenomena in two different coated systems subjected to scratch tests: (a) and (b) BSE and SEAM images of a 2000 gf scratch track ($\sim$250 μm ruby spherical slider) made in a 200 nm soft a:C-H coating deposited on (100) silicon by r.f. plasma-assisted CVD (25 kV, $\sim$230 kHz, β $\sim$4 μm); (c) and (d) similar images from a 5 μm thick 3-layer TiN/Ti/TiN coating on a tool steel (30 kV, $\sim$225 kHz, β $\sim$2 μm) clearly showing the progressive chipping and debonding at each interface. In both cases, the maximum amount of debonding is revealed at the edges of the scratch track [25–27].

blanking system (to modulate the electron beam close to its source in the column), a suitable sample holder incorporating a PZT detector from which an output signal is carefully extracted through a double-earthed electrical feed-through to the chamber, a small signal preamplifier (as close to the sample as possible) and a combined frequency generator (to drive the beam blanking system) with a phase-lock amplifier to detect those signals synchronously arising from the beam modulation. Careful earthing and screening arrangements are necessary to ensure that the signal detection chain only sees the output from the PZT rather than any residual beam current (the 'specimen current') flowing to earth from the sample. Finally, an additional video amplifier is usually required to match the resultant signals with the image display system. While a number of dedicated systems have been purpose built in various laboratories, we have used a commercial system supplied by Cambridge Technology (Cambridge, UK) capable of operating at frequencies in the 10 MHz–10 GHz range and originally based on that described by Davies [9].

Immediate potential problems relate to the detection of the very low contrast signal and its very low bandwidth inherent from the large capacitance of the PZT transducer. The signal output from the PZT (typically a disc of PZT5 (Morgan Co., UK)) is both at a low level and noisy but, after suitable pre-amplification, is usually sufficient to modulate the wave form monitor of the SEM at slow scan-line speeds (e.g., 40–100 ms. which requires slow scan imaging) with frame times of 40–240 s.

Having obtained and recorded standard secondary electron (or backscattered electron) images of the region of interest (e.g., a cracked area of coating, an indentation or a scratch/wear track), the beam-blanking system is activated and can be checked by the Moiré pattern created in a standard TV image (e.g., Fig. 8c when examined at typical SEM screen size). Then using very slow line scan waveforms in SEAM mode, the frequency range in which resonance of the particular sample holder is known to occur is swept through looking for contrast which occurs as very obvious maximum signals at well-defined, discrete operating frequencies and their harmonics and it is not unusual for there to be at least 6–8 such frequencies found for a 10 mm sample/PZT diameter in the frequency range 100–250 MHz. These frequencies are noted and images formed with each in turn having carefully adjusted the phase-lock amplifier for maximum detail and amplitude by both trimming the modulation frequency and sweeping the phase lag through 180°. A simple check that true

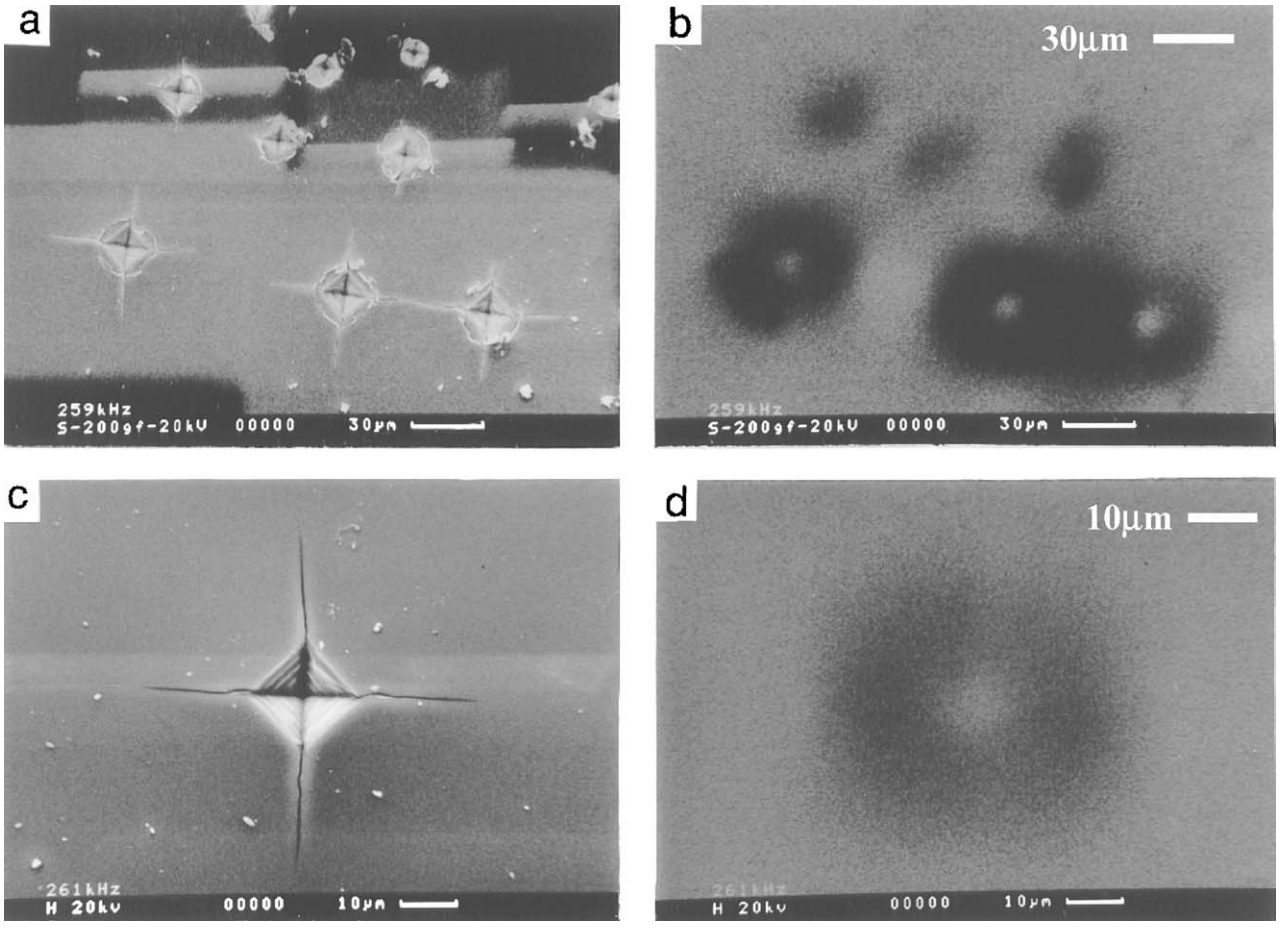

Figure 6 Example of the load-dependent indentation-induced fracture behaviour of a 200 nm hard carbon coating on (100) silicon [28]: (a), (b) a secondary electron-SEAM pair of an array of 50, 100 and 200 gf Vickers microindentations clearly showing the large extent of sub-surface coating debonding around the 100 gf and 200 gf—but not the 50 gf indentations (dark contrast in SEAM under the image conditions used). Thus SEAM readily allows the critical indentation load for coating debonding to be determined without through-thickness sectioning of the surfaces; (c), (d) similar images for a single 200 gf indentation (~260 kHz; 20 kV) [28], in which the interfacial debonding of the coating clearly revealed in (d) is not apparent in standard secondary electron image in (c).

SEAM contrast is occurring (rather than any anomalous charges (or specimen current) leaking to the PZT transducer) is to check that the image contrast does indeed completely reverse (on the wave form) with a phase shift of π and that there are other regions, $\pi/2$ away (from each and thus also 2π apart in phase) at which no signal is detected. Imaging conditions are then set for maximum contrast, integrated through the framestore for periods ranging from 10–30 frames and recorded for later processing and comparison with standard secondary electron or backscattered images. The final choice of display of contrast (e.g., black-on-white or *vv*) is in the hands of the operator. As was observed earlier [9], what is important is that contrast arises, not its sign which may change rapidly from one area on the sample to another.

Typical probe currents to obtain good contrast are of the order of 4×10^{-7}A—which for most SEM instruments is large—and this restricts the lateral resolution (as determined by the electron beam spot size) to ~ 1 μm. However, this is only of the order of the resolution limited by the beam spreading in the sample as the thermo-elastic conversion occurs.

3.3. Monte-Carlo modelling

A suite of Monte-Carlo modelling programs [23] was incorporated into the computer controlling the optical archive. Simple estimates of the electron range as a function of kV can thus be made, on-line, while imaging, which allows the operating voltage to be tailored to the microstructural scale, chemical identity and coating thickness of the sample. A typical abbreviated output is shown in Table I.

3.4. Samples

A wide range of gear steels and samples surface-engineered with thin hard coatings have been used in the present study ranging from small wafers of coated materials used for indentation and nanoindentation tests, through thin samples of material cut from larger coated samples, to materials cut from gear teeth. In all cases, the typical sample size was approximately 10×10 mm in area with thicknesses of 0.1–5 mm and the lower surfaces were lightly polished to remove course roughness such that the sample could be simply pushed against the upper face of a PZT detector in a spring-loaded sample holder and make good mechanical contact. The upper retaining plate of the sample holder (against which the imaged surface rests) also had good contact with the sample and was carefully grounded (to conduct the residual beam electrons (the specimen current) to earth). The output from the PZT disk was taken through separately screened leads

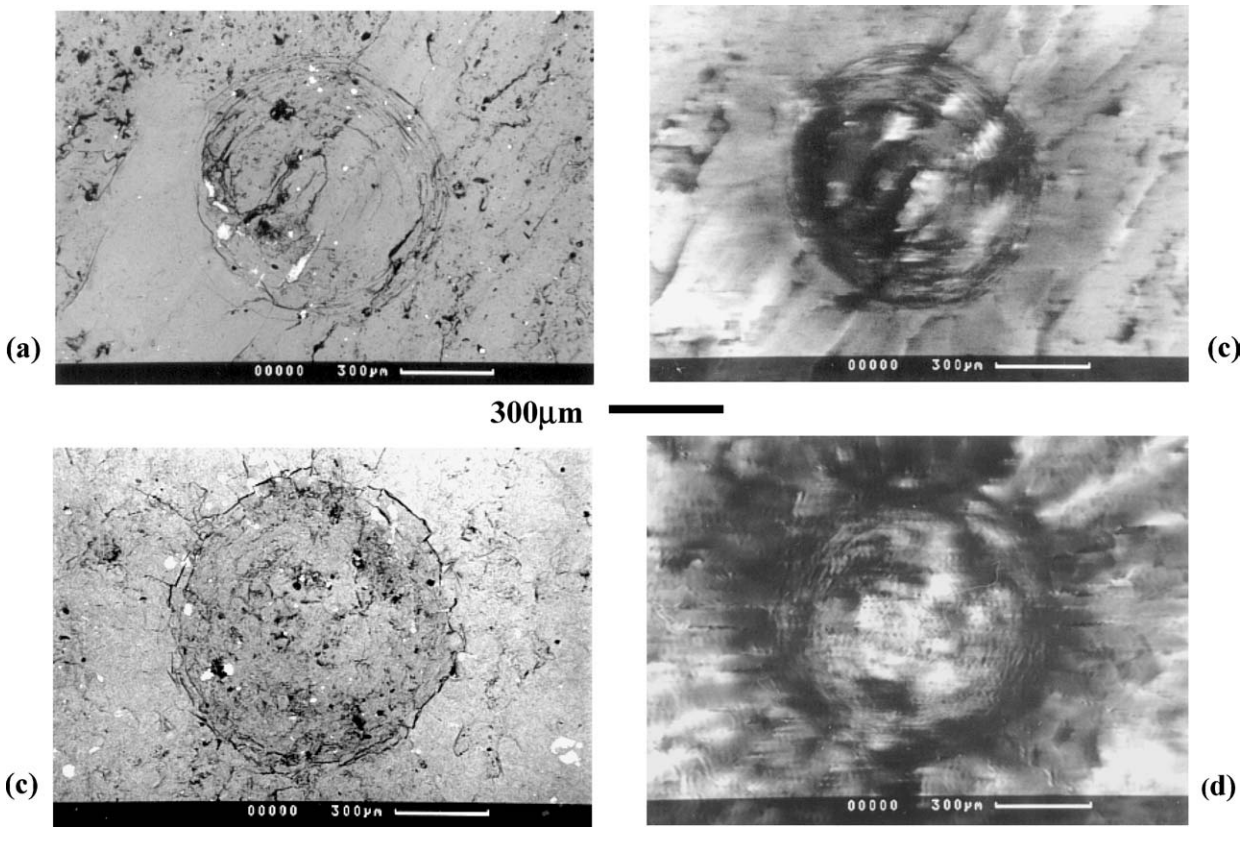

Figure 7 Backscattered electron images (BEI) and SEAM images of 2 kN indentations (made using a 2 mm diameter tungsten carbide ball) in 40 μm thick CrN coated stainless-steel samples with two different interlayers (a plasma nitrided layer in (a) and (b); an electroles nickel-coated layer in (c) and (d)). In each case, BEI in atomic number contrast mode shows surface cracking of the CrN, while SEAM shows subsurface decohesion of either the ceramic, or the interlayer, or both. (a) BEI reveals a small region where the CrN has spalled within the indentation crater; (b) SEAM of the same sample (25 kV; 147.1 kHz), showing that some of the coating has delaminated within the indentation, but that there is no delamination around the contact area; (c) BEI of Ni-interlayer sample; (d) SEAM of the same indentation (25 kV; 196.6 kHz), showing extensive delamination around the indentation, with a central region of adherent, plastically deformed coating. In both cases, there is some evidence of reduced SEAM contrast in the center after indentation suggesting that some campaction and densification of the porous coatings may have occurred. (The slight 'doubling' of the SEAM image is due to an electronic fault in the electrical connections to the sample) [29].

to a pre-amplifier on the outer wall of the sample chamber and thence to the phase-lock amplifier (see Fig. 1).

4. Results

The results which follow have been chosen to demonstrate the power of the SEAM technique for the study of the debonding and failure of thin coated systems together with the imaging of the extent of sub-surface fatigue cracks in gears.

4.1. The fracture behaviour of thin hard coatings

With regard to the study of coated systems, Fig. 3 shows three images from the same area of a sample of hard (M2) tool steel coated with ~5 μmTiN which has been subjected to a macro-indentation test with a WC ball indenter resulting in both through-thickness cracking and some obvious coating spallation around the periphery of the contact site. (The contact centre was above the upper edge of each figure). Fig. 3a (the secondary electron image) clearly shows the surface topography around the contact site, while Fig. 3b (the backscattered image in z-contrast mode) clearly reveals the TiN coating (mid-grey), the underlying steel substrate revealed where the coating has completely spalled (light grey), a number of through-thickness cracks in the coating and a number of small patches of the grey-imaging material (presumed residual, TiN fragments adherent to exposed carbides) on the steel surface in the debond area. Fig. 3c shows the SEAM image of this same area recorded at 203.2 kHz and clearly revealing areas of debond (presumed running along or close to the coating-substrate interface). E_o was chosen to be 20 kV, giving β ~2–3 μm in both Fe and TiN, such that the thermoelastic conversion would occur in the coating somewhere above the coating substrate interface: thus the dark areas in the Figure are presumed to be debond cracks. Interestingly, some of the residual TiN on the exposed steel surface shows dark contrast (and is thus assumed to be *loose*) while the remainder of the TiN particles shown in Fig. 3b are invisible [5, 8] and are assumed to still be *strongly bonded* to the substrate (i.e., providing no acoustic impedance). However, some may be too thin (i.e., thickness $\ll t_c$) to be providing contrast even if poorly bonded. Of further interest is the unexpected observation of a number of through-thickness cracks in the coating clearly revealed in the SEAM mode (and presumed to arise from these cracks providing additional nodes in the surface standing wave system) together with some mottled contrast across the whole surface (which it is tempting to believe is due to regions of good and bad adhesion of the coating overall—though we have yet to devise an experiment to independently

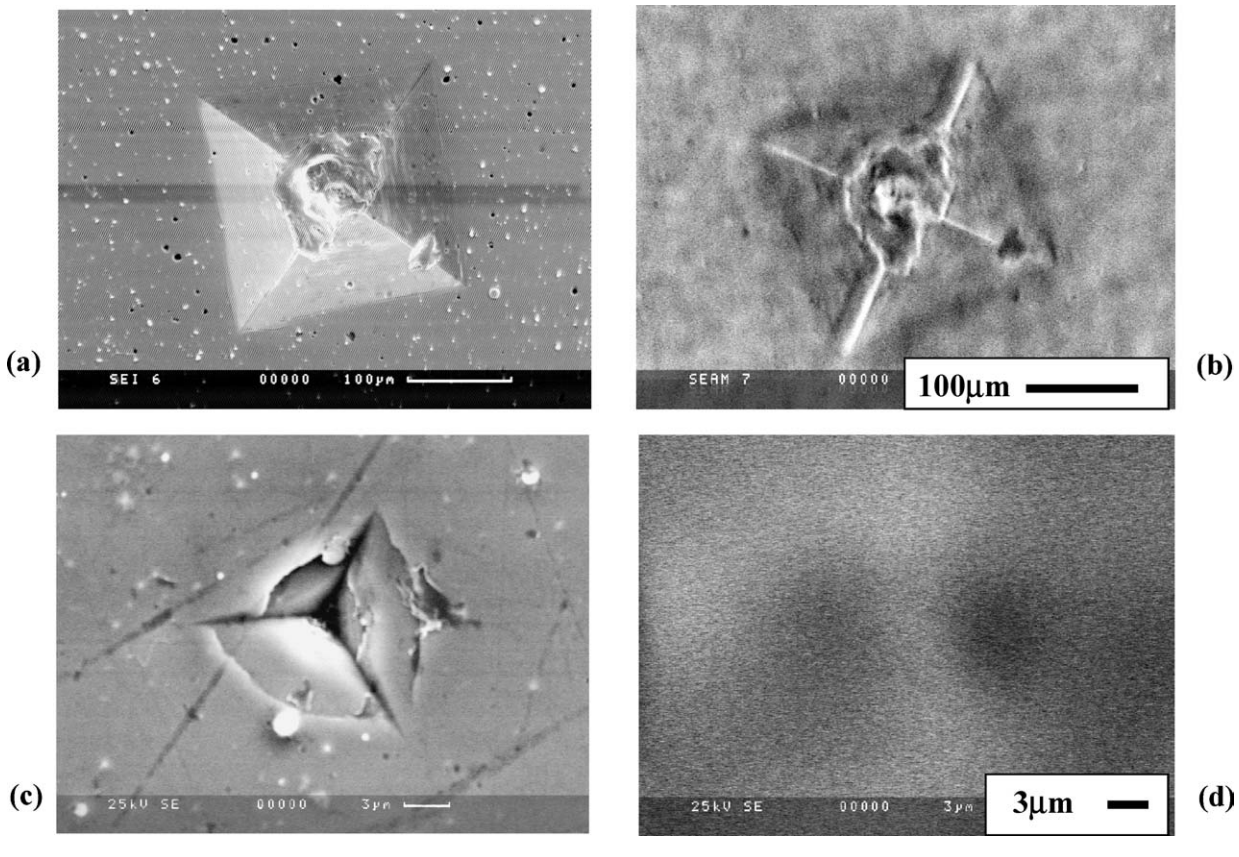

Figure 8 Secondary electron (SE) and scanning electron acoustic microscopy (SEAM) images of indentations made in a multilayered 4 μm-TiN/ZrN/coating on 304 L stainless-steel sample. (a) SE image of a 100 N macro-Vickers indentation with (b) a SEAM image of the same indentation showing dark contrast from the regions of coating-substrate debonding; (c) an SE image of a 500 mN nanoindentation (taken under different conditions of probe current and resolution) clearly suggesting that some coating decohesion may have occurred in this case, but not allowing the extent of any subsurface debonded region to be estimated with any precision; (d) SEAM image of the same area as in (c) clearly showing evidence of two areas of debonding each of a few square microns in extent. (The misshapen centre of the macro-vickers indentation is due to a badly chipped indenter tip) (25 kV, ~200 kHz for both (b) and (d)) [29].

confirm this). The setting of the phasing to show dark contrast for debond cracks parallel to, but below, the surface, is purely a subjective one and, given the nature of this microstructure, the most likely features to be providing strong contrast are cracks in the interfacial region. However, we know of no other technique which will so clearly delineate the extent of interfacial debonding at these scales of $\sim$10 μm or so.

In the early description of SEAM, we described that several resonances can be detected for any sample/holder combination. This is demonstrated in Fig. 4 which shows five SEAM images of the area shown in Fig. 3 but taken with different modulation frequencies to show how contrast, image content and image resolution vary widely (and somewhat unpredictably) with beam chopping rate. With Fig. 3c, these six images form three pairs of increasing frequency each with a further higher-frequency image taken at approximately double the modulation rate. Generally, the images recorded at higher frequency show the better lateral resolution. Also, both the number of dark imaging and 'invisible' debris particles on the exposed steel surface vary with frequency, suggesting that the depth-resolution is varying markedly, being generally greater at higher value of the chopping frequency. Further, the through-thickness cracks are more readily visible in some of these images than others as is the extent of the debonded area. Of ten images recorded at different frequencies for this sample, Fig. 3c was chosen as containing the best combination of image details of interest (debond areas, through-thickness cracks, loose debris etc.). Unfortunately, the contrast theory for this imaging mode is not sufficiently developed to offer explanations as to the detailed reasons for why the information content of these images differ: thus we would encourage other users to experimentally investigate all resonances occurring in the system and to find which contain the best information content.

With regard to contact damage around wear tracks and scratches in coated systems, Fig. 5 shows SEAM images of scratch tracks made on a 200 nm coating of a:C-H on (100) Si by r.f. plasma-assisted CVD [26] and a $\sim$5 μm thick 3-layer TiN/Ti coating on a hard steel [26]. In both cases SEAM clearly shows the extent of the debonding of all the interfaces involved. For the 1 μm a:C-H coating (heat treated to be in a soft condition [25, 27]), clear debonding contrast is seen in Fig. 5b while for the multilayer coating, areas of grey contrast (of approximately 20 μm width) can be seen emanating from all the interfaces involved. The very light contrast at the track bottom is probably simply due to the increased efficiency of the thermo-elastic

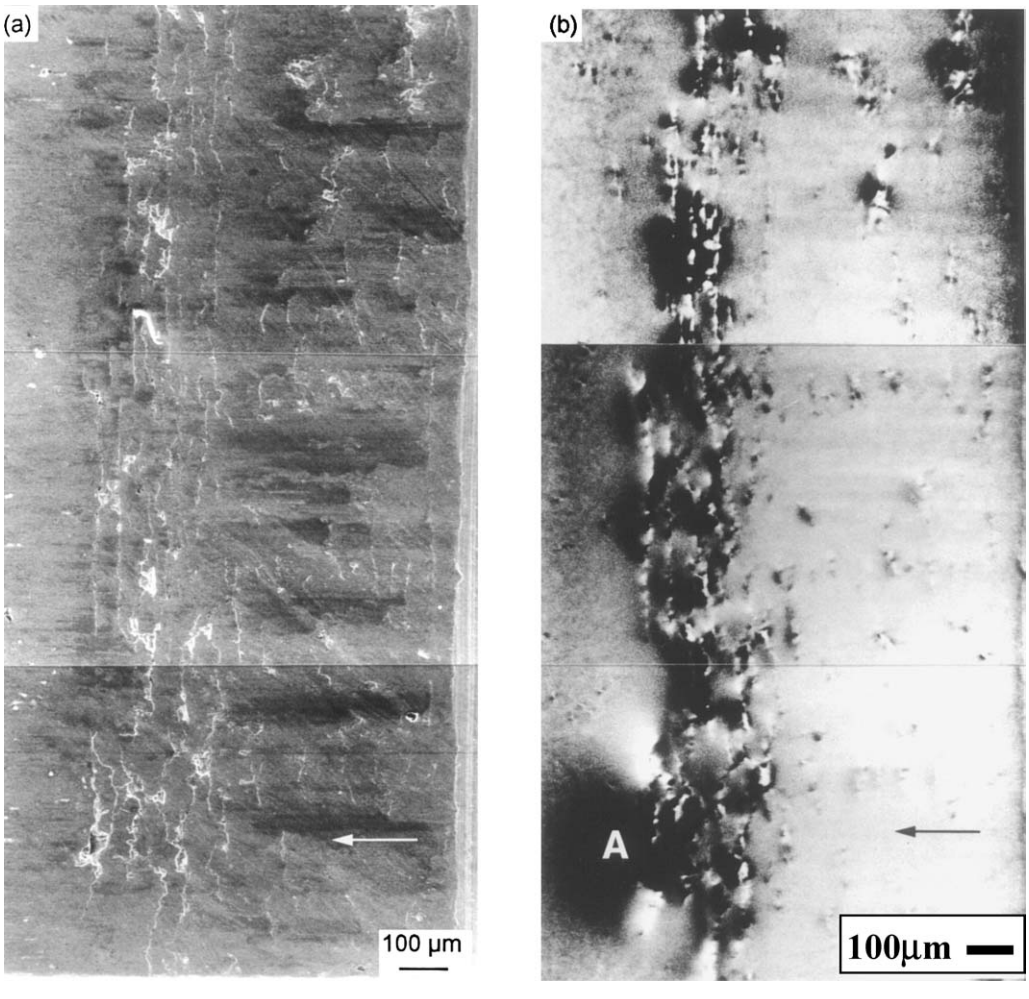

Figure 9 (a) Damaged gear tooth surface, imaged using secondary electron emission (SE) and showing copious surface-breaking pits and cracks; (b) Same area imaged using SEAM and showing that sub-surface cracks run into the sample in the direction of rolling (arrowed). As in Fig. 3c, the edges of the cracks at the surface show (unexpected) strong contrast in the SEAM image.

conversion in the steel substrate rather than the layered coating.

Since SEAM readily reveals the extent of sub-surface cracks (e.g., associated with the debonding of the coating-substrate interface) it can be invaluable in detecting critical indentation and scratch loads at which such debonding first occurs. For example, Fig. 6 shows secondary electron and SEAM images from 50, 100 and 250 gf microindentations in a harder version of the carbon coating on silicon shown in Fig. 5 [28]. The extent of subsurface cracks (presumed to run along the interface and acting as the precursor of total debonding of a significant area of the coating) is clearly visible. In (b) it is obvious that the 50 gf indentations show no debonding while the 100 and 200 gf ones do. Thus a critical debonding load/stress can be found experimentally—and without sectioning of the sample—*even though none of the debond cracks have yet broken out to the surface*. Without SEAM, such critical loads are measured to be somewhat higher if the onset of visible spalling on the surface is taken as the necessary criteria. Also, the debond contrast shows a minimum in (c) along the traces of the surface-breaking median cracks. This is a further example of free surfaces affecting SEAM contrast presumably by introducing constraints into the local wave pattern. Besides allowing us to refine our criteria for critical loads for debonding, such images, combined with indentation fracture mechanics models, have potential for allowing interfacial fracture toughness values to be evaluated [e.g., 25–27, 29].

SEAM is equally applicable to thicker ($\sim$100 μm) coatings where the thermo-elastic conversion occurs

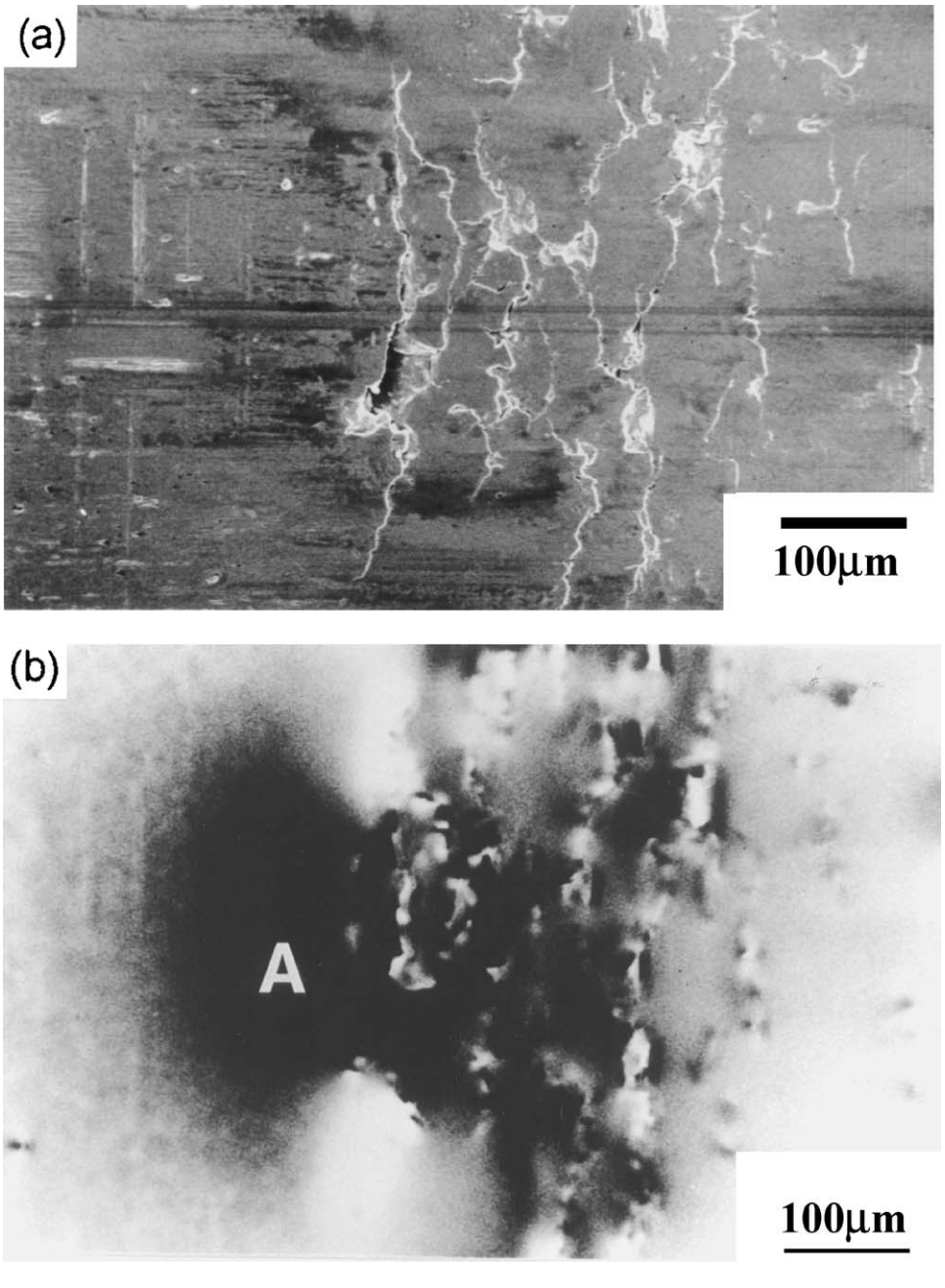

Figure 10 (a) Higher magnification view of the defect shown at A in Fig. 9 imaged using SE mode; (b) The same area imaged using SEAM. Note that the extent of the crack below the surface is not seen with SE contrast. Using SEAM, dark contrast can be seen adjacent to the surface cracks, clearly revealing the extent of the sub-surface crack beneath the surface and in the direction of rolling.

within the coating thickness even at higher operating voltages. Under these conditions, it seems that the presence of interfacial debonding and cracks within the coating (i.e., somewhat beyond the thermoeleastic conversion depth) still show clear contrast. Thus, Fig. 7 shows secondary electron and SEAM images of two ball indentations (2 kgf on a 400 μm sapphire ball) made into two different thermal-barrier-type ZrO_2 coatings on a nickel-base alloy. The image contrast here is complex, but essentially not only shows differences in the extent of debonding cracking of the coating but also a reduction in SEAM contrast due to those areas where the porous coating has compacted. That the two systems behave differently is clearly apparent and this is of critical importance in developing interfacial treatments to aid coating adhesion [30].

In order to test the ultimate special resolution of our SEAM system under real operating conditions, Fig. 8 demonstrates an attempt to obtain micron-level resolution from our SEAM system [29]. Fig. 8a and b shows secondary electron and SEAM images from a Vickers macroindentation in a TiN-coated steel system clearly showing debond areas within the indentation outline. Fig. 8c and d are a similar pair of images from around a 500 mN nanoindentation where, in order, to perform fracture mechanics calculations, the extent of any debonding beneath the indentation was a critical parameter. Even at this spatial scale (less than 1 μm)

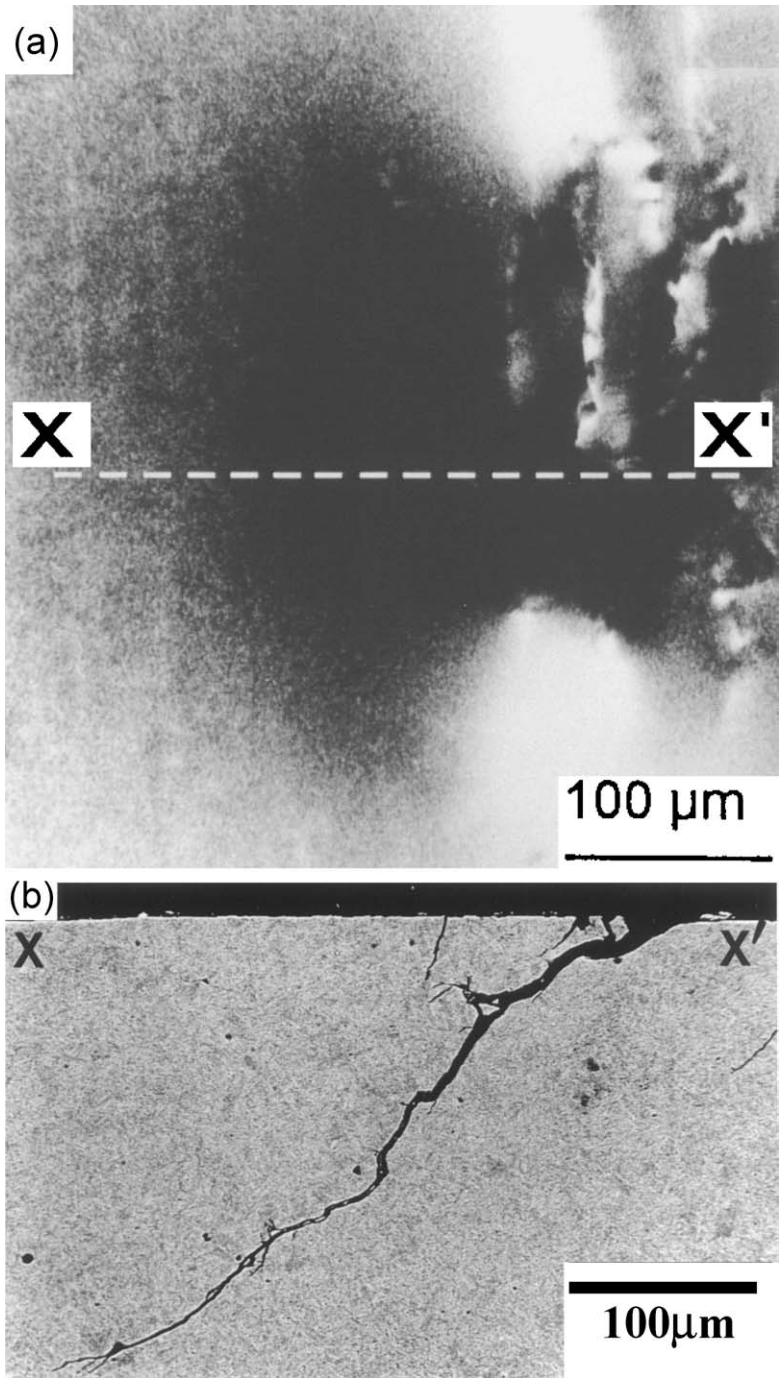

Figure 11 (a) Same area as in Fig. 10b after rotation of the specimen through 90° relative to the raster scan. Note that the contrast is unaffected by the rotation. (b) Metallographic section through plane XX′. Note the close correspondence between the horizontal extent of the microcrack and the size of the SEAM dark contrast.

which is close to the theoretical limit for the imaging system at 30 kV, some contrast is still clearly visible and establishes first that debonding has taken place on either side of the indentation and, second, that its extent is approximately 5 μm.

4.2. Contact fatigue in gears

Conventional macro-pitting damage was generated on the flanks of a carburised, steel gear by running a back-to-back gear test for 10^4 cycles are relatively high contact loads ($\sim$2.5 GPa mean Hertzian contact pressure). A representative tooth was then removed from the gear and sectioned through the central plane to produce a cut surface beneath the pitting damage where a PZT crystal, for acoustic detection, could be cemented giving a sample that could then be mounted in the usual way [7] for SEAM examination.

A region of the specimen surface imaged in conventional topographic (secondary electron) mode is shown in Fig. 9a. The surface shows a high density of microcracks, typical of the damage in gears run at a high load where lubrication may have broken down. Pits where material has flaked away are apparent in some areas. Fig. 9b shows the same area imaged using the SEAM technique. The microcracks visible with secondary electron imaging are also visible with SEAM, but, in addition, large elliptical areas of dark contrast are also visible. These areas were thought to indicate the presence of sub-surface microcracks lying on planes with a large component parallel to the surface of the specimen. While our images have been set to make dark contrast coincide with the presence of a crack, it is perfectly possible to reverse this and make the crack light and the surroundings dark.

A closer view of the defect labelled A in Fig. 9b is shown in Fig. 10. The extent of sub-surface cracking is clearly visible by the dark contrast in the SEAM image in Fig. 10b. However, to check that the contrast was not an artefact of either the SEM or SEAM technique, the specimen was rotated through 90° relative to the raster scan of the electron beam. The contrast was unaffected by the rotation, supporting the view that the contrast was produced by a real defect.

The contrast in Fig. 10b indicates that the size of the defect is about 150 μm in the direction of gear motion. A check on this was made by sectioning the specimen along the plane XX′ (Fig. 11a). This was done by mounting the specimen and grinding away material using silicon carbide paper initially, and 6 μm diamond slurry on a hard lap in the final stages. The accurate removal of metal was monitored by periodic examination of Vickers pyramidal diamond indents which were made on the specimen surface for use as depth gauges. A section through the defect A is shown in Fig. 11b. The sub-surface defect is in fact a continuation of the surface microcrack, which has grown down into the material and then turned to lie at an angle of about 30° to the surface plane. Comparison of Fig. 11a and b shows a good correlation between the horizontal component of the length of the defect: 150 μm from the SEAM contrast and 140 μm for the metallographic section.

Having proved the SEAM technique on surface-breaking cracks generated by conventional contact fatigue on gear teeth, SEAM has since been used to improve the understanding of the phenomenon of 'micropitting' which is now a common contact fatigue failure mode in high performance gearing where the progressive removal of material through small pit formation ultimately results in high vibrations and eventual tooth failure. This mode of failure is not well understood and there has been much debate over whether crack initiation has a surface or sub-surface origin. SEAM has shown that sub-surface crack growth is only found where cracks are surface breaking hence giving credibility to the assumption that surface initiation is the important controlling failure mechanism. These observations have helped to direct current research into the prevention of micropitting towards investigations into surface property modifications (e.g., surface finish, coatings and lubrication chemistry).

5. Discussion and conclusions

The results reported above confirm that the SEAM technique can be used to both detect and delineate the extent of sub-surface flaws generated by contact damage to coatings and by fatigue in gear wear. Since many of these cracks are virtually impossible to detect by other techniques, it is difficult to undertake exhaustive or critical confirmatory experiments to prove that the extent of the cracks and debonds etc. are as they appear in the SEAM image. However, our sectioning of gear teeth has demonstrated that the SEAM technique appears to be reliable in both detecting cracks and mapping their sub-surface extents. The only exception to this might be for cracks held tightly shut by residual compressive stresses where, by comparison with the signal enhancements experienced with the compacted coatings shown in Fig. 7, SEAM contrast might be either decreased or non-existent if little impedance is provided by the closed crack to the propagation of elastic waves.

The observation that only surface-breaking cracks were observed by SEAM in the micropitting studies raises the question as to whether or not cracks wholly contained beneath the surface—and perhaps held closed by local compressive stresses—could be detected. However, we note that conventional NDE techniques *can detect* wholly sub-surface cracks and, in the absence of better models for either SEAM image contrast or SEAM image simulations, we assume that SEAM would behave similarly. This view is supported by our indentation-based studies when images such as Fig. 6c and d confirm that wholly sub-surface cracks can indeed be detected.

With regard to resolution, our experiences show that resolutions typically compatible with that of a high-quality light microscope (i.e., $\sim$1 μm) are obtainable with care and if the best image is chosen from a carefully recorded sequence of different frequencies. As the theory predicts, the lateral resolutions we have observed certainly degrade with increasing the diameter of the incident electron beam and improve as images are recorded at higher chopping frequencies. However, on this latter point, this increase in lateral resolution with

frequency has to be seen as a *general trend* since the detailed content of a series of images recorded as different chopping frequencies on the same sample (e.g., Fig. 4) do show quite marked differences in image content between them even though the 'best resolution'—at least as judged by image acuity and detail—certainly appear at the higher chopping frequencies.

With regard to the depth sampled by the technique, the observations of the adherent debris on the exposed steel sections shown in Figs 3 and 4 certainly suggest that, as with lateral resolution, there is an increase in sensitivity to features lying closer to the surface as the chopping frequency is increased—that is more of the loose debris appears to be imaged at the higher frequencies. Since we have had to operate our SEM at E_o values of 20–25 kV (and above) in order to obtain sufficient gun brightnesses to generate SEAM images, we have not been able to explore in any detail the variation of information retrieval depth with E_o (i.e., with changing β, the electron range). However, the overall picture of SEAM sensitivity to a range of operating parameters is at least constant with the prediction of the background theory. We have not experienced the difficulties alluded to by Davies [9] in examining similar, but slightly thicker ($\sim$10 μm), TiN coatings to those used here and, since we have been able to image debonding cracks under much thicker coatings (e.g., Fig. 7), we have to conclude that Davies' difficulty was not wholly with thickness.

There seems to be an unexpected bonus with regard to trying to image surface-breaking cracks (e.g., the through-thickness crack shown in Figs 3 and 4, and the surface-breaking fatigue crack shown in Fig. 9) in that, as far as we can tell, we have been successful in imaging the cracks right up to the surface. This appears to be contrary to our expectation that such cracks would not provide image contrast when they lie at distances closer to surface than t_c–as certainly seems to be true with the loosely adherent debris discussed in the last paragraph. However, it does seem that surface-breaking cracks are delineated by strong contrast and this may be because they provide unexpected nodes in the surface vibrational wave pattern which other structural features (e.g., the loose debris in Figs 3 and 4) do not. The lessening of contrast displayed by the debond cracks in Fig. 6b and d as they approach the surface-breaking median cracks is interesting but we cannot determine whether this is caused by the debond actually failing to intersect the median or whether it is caused by a localised signal phase change again caused by the median cracks introducing local nodes into the acoustic wave pattern (as with the through-thickness cracks in Figs 3 and 4).

Sample sizes can currently be restrictive and all the samples here had to be extracted, destructively, from large samples in order to 'fit' the SEAM detector (even though the Camscan stage itself will easily accommodate a 200 mm gearwheel). However, Balk [21] has clearly demonstrated that SEAM transducers can be adapted to suit a variety of sample sizes and experimental environments (including temperature-variant imaging). Thus, this situation may change but, essentially, sample size and resonant frequencies scale with each other, and thus it may be impossible to form SEAM images with very large samples.

The observation (Figs 10 and 11) that SEAM contrast is independent of the orientation of the scanned raster on the sample, clearly demonstrates that the contrasts in all the images here arises from features within the sample and is not an artefact of interactions due to the scanning process itself.

There is obviously still an urgent need to further develop the physics of the contrast processes and thus place image analysis on a far more rigorous, quantitative and firm footing.

With regard to the lack of widespread application of the SEAM technique, we have to conclude that this is partly because of the lack of awareness of the research community of its possibilities in the contact-damage coatings areas. However, the fact that the contrast theory is both complex and poorly developed, together with the relatively high capital cost of the additional equipment ($\sim$\$100 k) may be a significant dissuation to many researchers though, following the results presented above, we believe that it is worth the investment to turn a routine SEM into having many of the capabilities of a scanning acoustic microscope for surface damage work. The images shown in Figs 3–7 clearly establish the benefits of SEAM images when recorded in parallel with images from other signals such that surface topography and atomic number distribution (i.e., chemical identity) can also be mapped.

We conclude that the SEAM technique seems capable of delivering contrast from information lying in a slice close to the sample surface with the sample depth straddling the electron range. The technique seems to work well for both metal and ceramics of a wide range of atomic number. Though thermoelastic conversion theory suggests that it would be increasingly difficult to retrieve information from progressively closer to the sample surface than this depth, we have been able to observe the traces of surface-breaking cracks and thus the technique is capable of providing information from a near-surface slice (which in some cases can extend right to the surface) without interference from features in the rest of the sample depth. This is in direct contrast to the SAM technique which samples the whole of the through-thickness of the sample. Obviously for surface-engineered systems (e.g., coatings and the study of surface damage) this is an *ideal situation* and one worthy of further exploitation. Indeed, SEAM has been critical in helping develop our understanding of micropitting.

As a result of our studies we would suggest that the following types of coatings and surfaces information now also be included in the list accessible by SEAM techniques as long as it can be experimentally arranged for the features of interest to be within $\sim t_c$ (or β) of the surface.

- revealing sub-surface debonding and decohesion of thin coatings
- delineating through-thickness coating cracks
- distinguishing loose debris
- detecting surface-breaking cracks

- identifying crack extents & inclinations to surfaces
- mapping the compaction of porous coatings.

Acknowledgements

The Newcastle Ceramics SEM was purchased, commissioned and developed with funding from the Materials Commission of SERC (now EPSRC), the University of Newcastle Equipment Fund and MRC. It is a pleasure to acknowledge the work of Dr. Sarah Hainsworth, Dr. Philip Ramsey, Dr. Peter Twigg, Dr. Joselyn Knight and Dr. Ray Barrett. Professor David Joy (University of Tennessee at Knoxville, USA) is thanked both for provision of the Monte-Carlo program suite and many helpful discussions. Messrs Camscan, Oxford Instruments, KE Developments, Link and Cambridge Technology are thanked for their assistance with various technical developments; FEI (Europe) are thanked for the provision of LaB_6 and CeB_6 emitters. Pippa Howard (Electrical Research Agency, Leatherhead) is thanked for obtaining Fig. 5c and d during our initial evaluation of the SEAM system on her instrument. Thanks to Jen McDonald and Dimitrios Lassithiotakis for helping prepare the manuscript.

References

1. R. GILMORE, in "Concise Encyclopedia of Materials Characterisation," edited by R. W. Cahn and E. Lifshin (Pergamon, Oxford, 1993) p. 4.
2. D. E. W. STONE and B. CLARKE, in "Concise Encyclopedia of Materials Characterisation," edited by R. W. Cahn and E. Lifshin (Pergamon, Oxford, 1993) p. 58.
3. G. A. D. BRIGGS, "Acoustic Microscopy" (Oxford University Press, Oxford, 1992).
4. D. E. NEWBURY, D. C. JOY, P. ECHLIN, C. E. FIORI and J. I. GOLDSTEIN, in "Advanced Scanning Electron Microscopy and Microanalysis" (Plenum, New York, 1986) p. 45.
5. T. F. PAGE, *Inst. Phy. Conf. Ser. (UK)* **138** (1993) 295.
6. F. I. HUMPHRIES, *J. Microscopy* **195** (1999) 170.
7. B. A. SHAW, J. T. EVANS and T. F. PAGE, *J. Mats. Sci. Letts.* **13** (1994) 1551.
8. T. F. PAGE, "Festschrift for Sir Robert Honeycombe," edited by J. A. Charles and G. C. Smith (The Institute of Materials, London, 1992) p. 337.
9. D. G. DAVIES, *Phil. Trans. Roy. Soc. Lond.* A **320** (1986) 243.
10. L. J. BALK, *Adv. Electron Electron. Phys.* **71** (1988) 1.
11. E. BRANDIS and A. ROSENCWAIG, *Appl. Phys. Lett.* **37** (1980) 98.
12. G. S. CARGILL, *Nature, Lond.* **286** (1980) 690.
13. A. ROSENCWAIG, in "Scanned Image Microscopy," edited by A. E. Ash (Academic Press, London, 1980) p. 291.
14. *Idem.*, *Scann. Electron. Microsc.* **IV** (SEM, Inc. Chicago) (1984) 1611.
15. L. J. BALK, M. DOMNIK and M. SCHÖTTLER, *Inst. Phys. Conf. Ser. (UK)* **93** (1988) 219.
16. G. S. CARGILL, in "Scanned Image Microscopy," edited by E. A. Ash (Academic Press, London, 1980) p. 319.
17. A. ROSENCWAIG, *Science* **218** (1982) 223.
18. A. ROSENCWAIG and R. M. WHITE, *Appl. Phys. Letts.* **38** (1981) 165.
19. M. K. THOMAS, R. C. FARROW and D. C. JOY, Bell Labs Report TM 82-11526-9 (1982).
20. D. C. JOY, *Inst. Phys. Conf. Series* **93** (1988) 23.
21. L. J. BALK, D. G. DAVIES and N. KULTSCHER, *Phys. Status Solidi* A **82** (1984) 23.
22. E. D. BOYES, *Inst. Phys. Conf. Ser.* **98** (1989) 439.
23. D. C. JOY, "Monte Carlo Modelling for Electron Microscopy and Microanalysis" (Oxford University Press, Oxford, 1995).
24. T. F. PAGE and P. M. RAMSEY, unpublished work.
25. J. C. KNIGHT, T. F. PAGE and H. W. CHANDLER, *Surf. Coat. Tech.* **49** (1991) 519.
26. P. M. RAMSEY and T. F. PAGE, unpublished work.
27. J. C. KNIGHT, T. F. PAGE, H. W. CHANDLER and P. M. RAMSEY in "Designing Ceramic Interfaces II," edited by S. D. Peteves (Official Publication of the EC, Physical Sciences EUR 15306, 1993) p. 253.
28. J. C. KNIGHT and T. F. PAGE, *Surf. Coat. Tech.* **53** (1992) 121.
29. S. V. HAINSWORTH, M. R. MCGURK and T. F. PAGE, *ibid.* **102** (1998) 97.
30. P. C. TWIGG and T. F. PAGE, *ibid.* **68/69** (1994) 453.

Received 3 December 2003
and accepted 20 January 2004